Magnetotransport properties and Shubnikov–de Haas oscillations in a Type-II nodal-line semimetal candidate n-type Mg_3Bi_2 single crystal

Yosuke Goto[1*], Masayuki Murata[1], Hidetomo Usui[2], Keigo Ono[1,3], Joseph P Heremans[4], Taichi Terashima[5], and Chul-Ho Lee[1]

[1]National Institute of Advanced Industrial Science and Technology (AIST), Tsukuba, Ibaraki, 305-8568, Japan
[2]Department of Applied Physics, Shimane University, Matsue, 690-8504, Japan
[3]Department of Applied Physics and Physico-Informatics, Faculty of Science and Technology, Keio University, Yokohama, Kanagawa 223-8522, Japan
[4]Department of Mechanical and Aerospace Engineering, The Ohio State University, Columbus, Ohio 43210, USA
[5]Research Center for Materials Nanoarchitectonics (MANA), National Institute for Materials Science (NIMS), Tsukuba, Ibaraki 305-0003, Japan

*E-mail: y.goto@aist.go.jp

Abstract

Mg_3Bi_2 is a candidate Type-II nodal-line semimetal (a novel category of topological semimetals). However, the exotic transport properties of Mg_3Bi_2 single crystals are yet to be elucidated. Herein, we report the magnetotransport properties of an n-type Mg_3Bi_2 single crystal grown from a melt. The results revealed that the single crystal exhibited a very large nonsaturating magnetoresistance (5000%) under an 8 T field, significantly exceeding that of polycrystals. The combined analysis of Shubnikov–de Haas (SdH) oscillations, Hall resistivity, and first-principles calculations suggest that SdH oscillations originate from trivial electron bands rather than hole bands, which contain an almost linear dispersion. We confirmed that the electron mobility reached 10000 cm^2/Vs by analyzing Hall resistivity and magnetoresistance based on a two-band model. The electron/hole concentration and mobility were used to investigate the measured transport properties, such as the Nernst coefficient. Overall, these results are critical for elucidating the electronic structure and transport properties of Mg_3Bi_2.

Introduction

Topological semimetals and metals exhibiting nontrivial band crossings in their low-energy band structures have become a focus of recent research in the field of condensed-matter physics [1,2]. Among them, nodal-line semimetals represent a novel category of topological semimetals that are distinct from Weyl and Dirac semimetals, as they host closed loops or open curves of band degeneracy within the Brillouin zone [3-7]. Dissimilar to the massless electrons observed in Weyl and Dirac semimetals, the low-energy excitations of nodal-line semimetals exhibit very high masses along the tangent direction of the nodal lines and exhibit masslessness along the transverse directions in the momentum space. Additionally, nodal-line semimetals can be classified as Type-I or II based on the slope of the crossing band [8,9]. Type-I and Type-II nodal-line semimetals exhibit band crossings that are formed by two bands dispersed in opposite and the same directions, respectively. To date, most nodal-line semimetals are conventional Type-I, including the experimentally identified $PbTaSe_2$ [10], $PtSn_4$ [11], $SrAs_3$ [12,13], and ZrSiX (X = S, Se, Te) [14-17]. Type-II nodal-line semimetals are expected to exhibit marked differences in magnetic, optical, and transport responses compared with their Type-I counterparts. Notably, the compound, K_4P_3, is the first to be theoretically categorized as a Type-II nodal-line semimetal. However, its actual character has not been experimentally confirmed owing to its extreme air sensitivity [8].

Recently, Mg_3Bi_2 was explored as a Type-II nodal-line semimetal [9,18] as well as a high-performance thermoelectric material [19-24]. Angle-resolved photoemission spectroscopy was used to demonstrate that the tilted nodal-line forms a closed loop centered at the Γ point and that the drumhead-surface band appears inside the loop of bulk nodes [9]. Large magnetoresistance (MR) values, reaching 940% under a 14 T field, have been reported even for polycrystalline forms [25,26]. The synthesis of Mg_3Bi_2 single crystals can offer valuable insights into their detailed physical properties. However, the MR of Mg_3Bi_2 single crystals exhibiting the p-type polarity was only 3% at 2 K and 9 T [27] despite an expectation that single crystals exhibit higher MR values than polycrystals owing to their higher carrier mobilities. The unexpected result was most likely attributable to the locations of the nontrivial band crossing and nodal-line, which are slightly above the Fermi level in the typical sample [27-30]. Notably, n-type Mg_3Bi_2 single crystal synthesis is not straightforward, as excess Bi is typically used as a flux for growing crystals, and this results in p-type materials with Mg vacancies [27]. Several researchers have recently reported the synthesis of n-type Mg_3Bi_2 single crystals based on the suppression of Mg vacancies [24,31,32]. We have also reported melt-grown Mg_3Bi_2 single crystals with controlled Fermi levels and demonstrated their axis-dependent conduction polarity, i.e., their electrons mainly accounted for carrier conduction in the in-plane direction, whereas their cross-plane direction was dominated by holes [33]. However, their magnetotransport properties and Shubnikov–de Haas (SdH) oscillation have not been experimentally investigated.

Thus, we report the magnetotransport properties of n-type Mg_3Bi_2 single crystals. We confirmed that these crystals exhibited larger MR values than polycrystals (>5000% at 8 T), accompanied by a Shubnikov–de Haas (SdH) oscillation, for the first time. Although the

observed phenomena included a small effective mass and a possible nontrivial phase shift (ϕ), which could be signs of Dirac fermions, isotropic SdH frequency and Hall resistivity (ρ_{yx}) measurements suggested that SdH oscillations actually came from trivial electron bands along the L^*–M^* line, rather than from hole bands at around a Γ point with almost linear dispersion. The nonlinear ρ_{yx} and MR were analyzed using a two-band model, revealing that the electron mobility reached 10,000 cm^2/Vs at 4.2 K. The electron/hole concentration and mobility were used to reproduce and discuss the experimental observation of the Nernst coefficient.

Experiments

The melt-grown Mg_3Bi_2 single crystals were synthesized using Mg (4N, shot) and Bi (6N, shot) as starting materials as a Mg:Bi molar ratio of 3.05:2. They were loaded into a graphite crucible encapsulated in an Ar-gas-filled screw-top stainless-steel container and heated at 890°C for 48 h, cooled to 660°C at 2°C/h, and quenched to room temperature (20–25°C).

The chemical compositions were analyzed using a scanning electron microscope (TM-4000, Hitachi) equipped with an energy-dispersive X-ray spectroscopy (EDX) apparatus (Oxford). Synchrotron powder X-ray diffraction (SXRD) was measured at BL02B2 of SPring-8 (proposal number 2024A1635). The diffraction data were obtained using a high-resolution one-dimensional semiconductor detector (MYTHEN) [34]. The wavelength of the radiation beam (0.497199(1) Å) was determined using a CeO_2 standard. The crystal-structure parameters were refined by the Rietveld method using RIETAN-FP [35]. Laboratory X-ray diffraction (XRD) patterns were collected with CuKα1 radiation generated at 40 kV and 45 mA (SmartLab, Rigaku).

Thermoelectric transport properties were measured using a Gifford–McMahon refrigerator equipped with a superconducting magnet. The measurements proceeded with a 2 × 2 × 8 mm^3 sample. The electrical resistivity was measured using the four-probe method comprising the attachment of Cu wires (diameter: 25 μm) to an Ag-based epoxy. The temperature difference along the sample was generated by a small 120 Ω heater. Copper–constantan thermocouples were used to determine the temperature variations, and the Seebeck coefficients (S) were obtained from the plots of the thermopower values generated between the Cu wires as a function of the temperature drop, whereas the thermal conductivities (κ) were determined by plotting the heater power against the temperature drop. To measure the Hall resistivity (ρ_{yx}) and the Nernst coefficient (N), we attached an additional set of copper wires in the transverse direction to the heat flow and applied magnetic field (B).

First-principles calculations based on density functional theory, including spin–orbit coupling, were performed using the WIEN2k software package [36] together with the modified Becke–Johnson potential [37,38]. The experimental crystal structure employed in these calculations was obtained from a previous study [39], whereas RK_{max} and k-mesh values were set to 8 and 15 × 15 × 8, respectively.

Results and Discussion

Zero-field transport properties

The results of the EDX-based elemental mapping shown in Fig. S2 confirm the homogeneous distribution of Mg and Bi in the sample [40] (see also reference [1] therein). Chemical composition analysis revealed a Mg:Bi molar ratio of 59.0(1):41.0(1), which was very close to the expected stoichiometric value. The SXRD patterns and Rietveld-refinement results are shown in Fig. S3. Most of the diffraction peaks were associated with space group *P*-3*m*1, indicating that the Mg_3Bi_2 exhibited a primary phase. The lattice parameters were determined as follows: a = 4.65427(4) Å and c = 7.38781(9) Å, corresponding to the literature results [39]. Additionally, we observed weak peaks that were attributable to the impurity-phase Bi (1.9 wt%). However, this is probably because of surface decomposition during sample handling process. Laboratory powder XRD of Mg_3Bi_2 with different exposure time to the ambient air is shown in Fig. S4. Diffraction peaks due to Bi impurity were not observed for the fresh sample. They appeared only after several hours of exposure time.

Figure 1(a) shows the temperature (T) dependence of the in-plane and cross-plane electrical resistivities (ρ_{xx} and ρ_{zz}) of the zero fields. At T = 300 K, ρ_{xx} and ρ_{zz} were 20 μΩm, which decrease with decreasing T. The anisotropy in ρ_{xx} and ρ_{zz} was negligible. The residual resistivity ratios (RRR), ρ(300 K)/ρ(4.2 K), for ρ_{xx} and ρ_{zz} were significantly high (23 and 26, respectively), reflecting the high quality of the crystals explored here. Further, ρ_{xx} and ρ_{zz} followed the T^2 dependence below 20 K (Fig. 1(b)), probably because of electron–electron or electron–phonon scattering in low-carrier systems [41,42]. The temperature dependence of κ also exhibits an almost isotropic behavior, as shown in Fig. S5. Conversely, the in-plane and cross-plane Seebeck coefficients (S_{xx} and S_{zz}) exhibits anisotropic properties (Fig. 1(c)). Notably, the 300 K S_{xx} and S_{zz} were determined as −133 and −88 μV/K, respectively, because of the band anisotropies of the conduction and valence bands, as previously demonstrated [33].

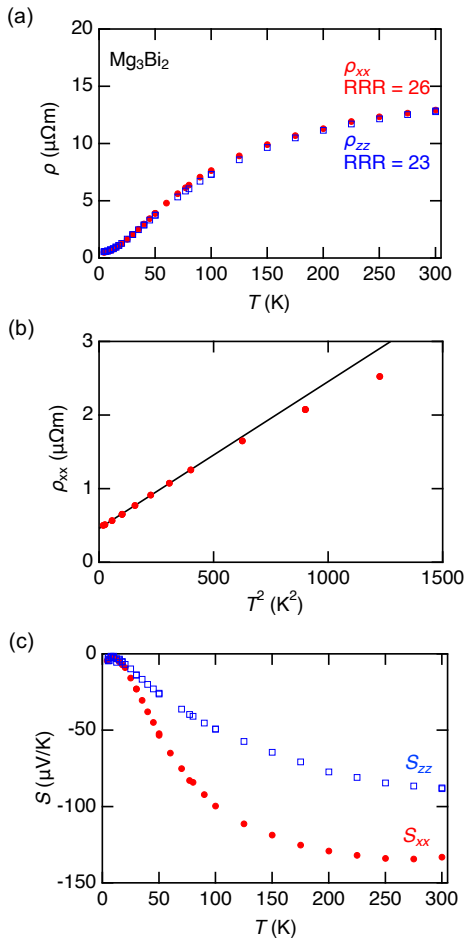

FIG. 1. (a) T dependence of ρ_{xx} and ρ_{zz} for Mg_3Bi_2. RRR is denoted in the inset. (b) ρ_{xx} vs. T^2 below 35 K. The black solid line represents the linear fit below 20 K. (c) S_{xx} and S_{zz} vs. T.

Magnetoresistance and SdH oscillation

Figure 2(a) shows the MR ratio, $[\rho_{xx}(B) - \rho_{xx}(0)]/\rho_{xx}(0) \times 100$, along the in-plane direction as a function of the B up to 8 T at 3.2–20 K with an applied field along the c-axis (i.e., $B \perp ab$ plane). MR increases with the increasing B, reaching 5000% at 3.2 K and 8 T, which is much higher than that of polycrystals [25]. Furthermore, we observed the MR oscillations in the High-B region along with the smooth background, i.e., the SdH oscillation. By subtracting a polynomial background of ρ_{xx}, the SdH oscillation periodic in $1/B$ can be resolved from as low as 3 T (Fig. 2(b)). Notably, this is the first report of the observation of the SdH oscillation in Mg_3Bi_2.

The Fourier transform spectrum of the SdH oscillations as a function of $1/B$ at 3.2 K (see the inset in Fig. 2(b)) reveals a single oscillation frequency, $F = 29.2$ T, for B // c, corresponding to the periodicity $(1/B) = 0.034$ T^{-1}. Employing the Onsager relation, $F = (\hbar/2\pi e)S_F$ (where $\hbar$ is the reduced Planck's constant and S_F a cross-sectional area of the Fermi surface normal to the field), we obtained $S_F = 2.79 \times 10^{-3}$ Å^{-2}. Despite the strong angular dependence of the amplitude, the nearly unchanged oscillation periodicity for B // ab indicated that the Fermi sphere exhibited

negligible anisotropy (Fig. S7). Thus, by assuming a circular cross-section, a very small Fermi-wave vector (k_F = 0.030 Å^{-1}) was estimated. The Fermi surface obtained by first-principles calculations is shown in Fig. 4, and the calculated S_F is summarized in Table S1. Based on the isotropic electron pockets along the L*–M* line and the anisotropic hole pocket at the Γ point in Mg_3Bi_2, the SdH frequency seemed to arise from the electron rather than the hole. Using the relationship between k_F and carrier concentration (n), $k_F = (3\pi^2 n)^{1/3}$, and the six degeneracy of the electron pocket, n was calculated at 5.4 × 10^{18} cm^{-3}. This agreed reasonably with n obtained from the two-band analysis of ρ_{xx} and ρ_{yx} under a magnetic field, which is discussed later in this paper.

We note that the sample in the present study may contain the small amount of Bi impurity (Fig. S3), which may exhibit SdH oscillation from a low magnetic field. However, the smallest SdH periods in Bi are 0.51 × 10^{-5} G^{-1} (electron, B // binary axis) or 0.48 × 10^{-5} G^{-1} (hole, B in the trigonal plane) [43]. These correspond to F = 19.6 and 20.8 T, respectively. This is distinctly different from the frequencies observed in the present study: we observed about 5 oscillation periods between 1/B = 0.125 and 0.3 T^{-1} (Fig. 2(b)). If the frequency were 20.8 T, there would be only 3.6 periods in this field range. Clearly, the oscillation that we observed cannot be ascribed to the above frequencies of Bi. Furthermore, we add that we did not observe smaller frequencies from electron pockets of Bi, which are easier to observe, as observed by Shubnikov and de Haas in 1930 [44]. Therefore, we can safely conclude that the SdH oscillation arises from Mg_3Bi_2 rather than Bi impurity.

The SdH oscillation of the resistivity $\Delta\rho_{xx}$ can be described using the Lifshiz–Kosevich (LK) formula [44-46]:

$$\frac{\Delta\rho_{xx}}{\rho_0} = -C\sqrt{B}R_T R_D R_s \cos\left[2\pi\left(\frac{F}{B} - \frac{1}{2}\right) + \phi_D + \phi_B\right] \qquad (1)$$

where ρ_0 is the background resistivity, C is a positive coefficient, and we neglect harmonics. We have assumed that the electrical conductivity $\sigma_{xx} = \rho_{xx}/(\rho_{xx}^2 + \rho_{yx}^2) \approx \rho_{xx}^{-1}$ as ρ_{yx} was much smaller than ρ_{xx}. The temperature and Dingle reduction factors are given by $R_T = X/\sin hX$ and $R_D = \exp(-X_D)$, where $X_{(D)} = K\mu^* T_{(D)}/B$, $\mu^* = m_c^*/m_0$, and the coefficient K is 14.69 T/K. m_c^* and m_0 are the effective cyclotron mass and bare electron mass, respectively. The Dingle temperature T_D is inversely proportional to the carrier scattering time τ: $T_D = \hbar/2\pi k_B\tau$. The spin reduction factor R_s describes the interference of oscillations from up- and down-spin electrons and is given by $R_s = \cos(\pi g\mu^*/2)$, where g is the spin g factor. ϕ_D is $+\pi/4$ or $-\pi/4$ with the oscillation from a minimum or maximum cross-section of a three-dimensional (3D) FS pocket, respectively. ϕ_B is the Berry phase, which is 0 for normal electrons but π for Dirac fermions [47,48]. Because of the maximum cross-section of the 3D FS, the total phase shift, given by $\phi = \phi_D + \phi_B$, was expected to be $3\pi/4$ when Mg_3Bi_2 exhibited a Dirac fermion nature.

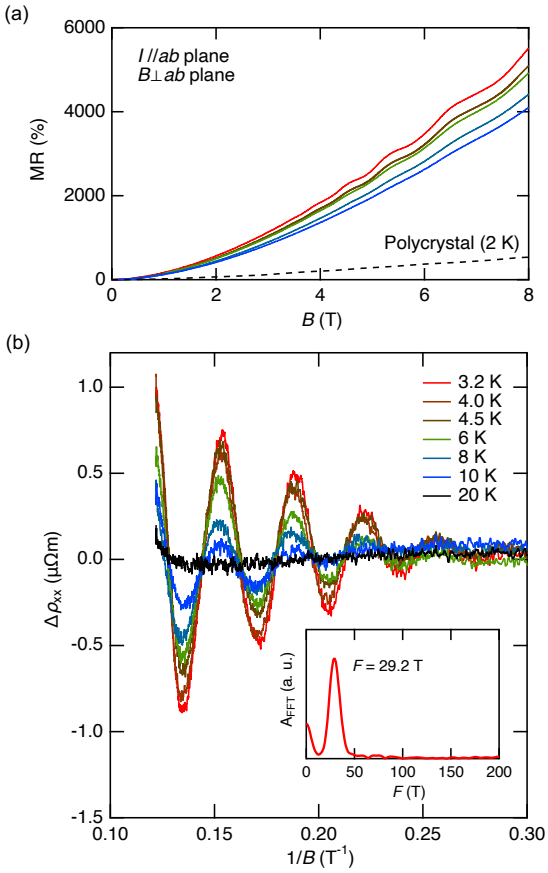

FIG. 2. (a) In-plane MR vs. B of Mg_3Bi_2 up to 8 T at T of 3.2–8 K. MR of the polycrystal at 2 K is also shown for comparison [25]. (b) Oscillatory component of MR ($\Delta\rho_{xx}$) vs. $1/B$ at various T. The inset shows the FFT spectrum of the SdH oscillations at 3.2 K.

Figure 3(a) shows the T dependence of the relative oscillatory component ($\Delta\rho_{xx}/\rho_0$) for the peak at $1/B = 0.135$ T^{-1}. The fit yields $m_c^* \sim 0.16\ m_0$. Thereafter, the Fermi velocity (v_F) = $\hbar k_F/m^*$ is obtained as 2.16×10^5 m/s. Fig. 3(b) shows the field dependence of the oscillation amplitude in the form of a Dingle plot. T_D and τ were estimated from the slope of the fit line, yielding 3.3 K and 369 fs, respectively. The estimated mean free path ($l = v_F \tau$) and quantum mobility ($\mu_q = e\tau/m^*$) were 80 nm and 4060 cm^2/Vs, respectively.

Next, we evaluated ϕ in Mg_3Bi_2 to examine the nontrivial π-Berry phase, which is considered a hallmark of various Dirac materials [49-52]. ϕ can be determined either directly from the fit to the LK formula (Eq. (1)) or the Landau level (LL) index plot. As shown in Fig. 3(c), the LK fit of the SdH oscillation yielded the phase shift of $\phi = 3.59(2)$, assuming $R_s > 0$. In addition, to obtain the LL-index plot, we assigned LL integer indices (n) and half indices ($n + ½$) to the minima and maxima in the oscillatory component of magnetoconductivity ($\Delta\sigma_{xx}$), respectively, as shown in Fig. S8 [53]. The nth minimum in $\Delta\sigma_{xx}$ satisfies the following relation:

$$2\pi\left(\frac{F}{B}-\frac{1}{2}\right)+\phi_D+\phi_B=(2n-1)\pi. \qquad (2)$$

Thus, the n vs. $1/B$ plot yields a straight line with F and $\phi=\phi_D+\phi_B$, corresponding to the slope and intercept on the n-axis, respectively. The best-fit straight line in the LL-index plot yields n-axis intercepts of 0.54(3), corresponding to ϕ = 3.39(3).

However, concluding the correct phase is not straightforward [54,55]. First, we must determine the sign of the spin reduction factor R_s. This is because the phase of the SdH oscillation is the same for normal fermions with negative R_s and Dirac fermions with positive R_s. The spin g factor may substantially deviate from the free-electron value g = 2, especially for small orbits. For example, for the Zn needle, g > 100 is generally accepted [44]. g can be determined using, for example, the spin-zero method in some special cases, but it is impossible in many cases [46]. Although R_s was assumed to be positive in this study, further study is needed to clarify the correct phase of Mg_3Bi_2.

Recently, the temperature dependence of the SdH frequency F has been used as a diagnostic tool for the nontrivial nature of bands [56–58]. As previously demonstrated in other material systems, including Cd_3As_2, $Bi_{1-x}Sb_x$, and CaFeAsF, topologically trivial bands have $dF(T)/dT \geq 0$, and those with Dirac fermions have $dF(T)/dT < 0$ [56]. This is because Dirac fermions have finite energy derivative values of the cyclotron mass due to the linear dispersion of the bands. Specifically [56],

$$F(T)=F_0-\frac{(\pi k_B T)^2}{4\beta}\frac{1}{m^*}\left|\frac{\partial m^*}{\partial E}\right|=F_0-\Theta\left(\frac{\pi k_B}{\mu_B}\right)^2\frac{T^2(\mu^*)^2}{F_0}, \qquad (3)$$

where F_0 is the frequency at T = 0, $\beta=e\hbar/(2m^*)$, and μ_B is the Bohr magneton. Θ is the sum of the topological part Θ^T = 1/16 and the Sommerfeld part Θ^S due to the temperature dependence of the chemical potential (Sommerfeld correction). Figure S9 shows the T dependence of F for Mg_3Bi_2, where F was obtained using the LK fit for $\Delta\rho_{xx}$. Unfortunately, the experimental uncertainty was larger than the expected frequency shift at ~0.1 T. SdH measurements at higher temperatures may thus be required to precisely determine the frequency shift.

Previous studies have predicted the existence of a nodal line in Mg_3Bi_2 from first-principles calculations without spin–orbit coupling [9,18]. However, as shown in Fig. 4, the band structure calculated with spin–orbit coupling has a gap (35 meV) around the Γ point, as reported in previous reports [9,18]. These results indicate that the spin–orbit coupling turned the bands around the Γ point into trivial bands, although the dispersion close to the gap was still nearly linear. It is possible to exploit a nontrivial band in transport properties by shifting the Fermi level upward. We noted that the band shape around the Γ point and the relative positions of the hole and electron pockets were different from those in previous calculations [9, 18]. This was because a different exchange–correlation potential was used in this study to reproduce the small Fermi pockets observed in the experiments. The calculated cyclotron mass of the electron pocket from the relationship $m_c^*=\frac{\hbar^2}{2\pi}\frac{\partial S_F}{\partial \varepsilon}$ was $0.20m_0$, which was in reasonable agreement with the experimentally observed value. In addition, topologically trivial Bi_2O_2Se reportedly showed a π-

phase shift probably due to large spin–orbit coupling, although no frequency shift associated with the linear band was observed, as expected [56]. We deduced that Mg_3Bi_2 in this study might be similar to the case of Bi_2O_2Se.

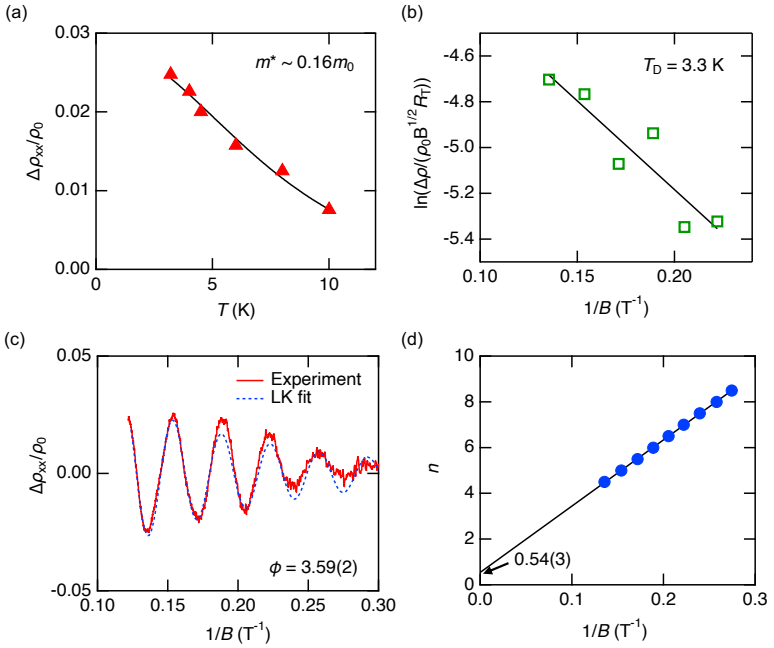

FIG. 3. (a) Oscillation amplitudes ($\Delta\rho_{xx}/\rho_0$) vs. T for the peak at $1/B = 0.135$ T^{-1}. (b) Dingle plot of the SdH oscillations with the oscillation frequency (F) = 29.2 T. (c) $\Delta\rho_{xx}/\rho_0$ vs. $1/B$ fitted to the LK formula. (d) LL-index plot.

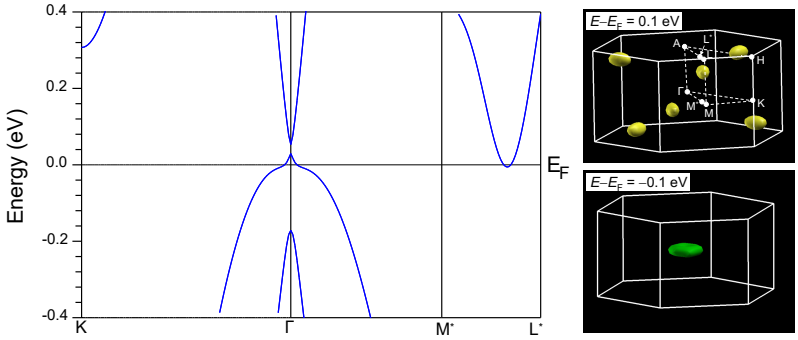

FIG. 4. Band dispersion near the Fermi level (E_F) and Fermi surface of the electron and hole pockets of Mg_3Bi_2. For visibility, the pockets were enlarged by shifting the band energies by +/−0.1 eV; otherwise, they would have been too small to see in the figures [33].

Two-band analyses

Figure 5(a) shows ρ_{yx} versus B at different Ts. The linear ρ_{yx} was observed up to 5 T above 50 K. Contrarily, the nonlinear ρ_{yx} and large MR ratio observed below 30 K indicated a two-band transport behavior, which can be described as follows [59–61]:

$$\rho_{yx} = \frac{1}{e}\frac{\left(n_{\mathrm{h}}\mu_{\mathrm{h}}^2 - n_{\mathrm{e}}\mu_{\mathrm{e}}^2\right) + \mu_{\mathrm{h}}^2\mu_{\mathrm{e}}^2B^2(n_{\mathrm{h}} - n_{\mathrm{e}})}{(n_{\mathrm{h}}\mu_{\mathrm{h}} + n_{\mathrm{e}}\mu_{\mathrm{e}})^2 + \mu_{\mathrm{h}}^2\mu_{\mathrm{e}}^2B^2(n_{\mathrm{h}} - n_{\mathrm{e}})^2}B \qquad (4)$$

$$\rho_{xx} = \frac{1}{e}\frac{(n_{\mathrm{h}}\mu_{\mathrm{h}} - n_{\mathrm{e}}\mu_{\mathrm{e}}) + \left(n_{\mathrm{e}}\mu_{\mathrm{e}}\mu_{\mathrm{h}}^2 + n_{\mathrm{h}}\mu_{\mathrm{h}}\mu_{\mathrm{e}}^2\right)B^2}{(n_{\mathrm{h}}\mu_{\mathrm{h}} + n_{\mathrm{e}}\mu_{\mathrm{e}})^2 + \mu_{\mathrm{h}}^2\mu_{\mathrm{e}}^2B^2(n_{\mathrm{h}} - n_{\mathrm{e}})^2}, \qquad (5)$$

where n_{e} (n_{h}) and μ_{e} (μ_{h}) are the carrier concentration and mobility of electrons (holes), respectively. As shown in Fig. 5(b and c), the fitting results obtained using Eq (3,4) were reasonable, although the MR in the High-B region was not well captured. The obtained n_{e} (n_{h}) and μ_{e} (μ_{h}) values are shown in Fig. 5(d and e). The similar values obtained for n_e and n_h are consistent with the semimetallic nature of Mg_3Bi_2. Notably, μ_{e} and μ_{h} reached 1.02×10^4 and 0.83×10^4 cm^2/Vs, respectively, at 4.2 K. A higher electron than hole mobility ($\mu_{\mathrm{e}} > \mu_{\mathrm{h}}$) corresponds to a negative slope of the Hall curve in the low-B region, turning into a positive slope owing to the existence of a lower-mobility hole. Therefore, we consider that the observed SdH oscillation is due to the electron (i.e., with higher mobility. The charge carrier concentration and mobility above 50 K are not depicted in Fig. 5(d and e) because the linear ρ_{yx} behavior is not suitable for two-band analysis with Eqs (3) and (4). Measurements under higher magnetic fields are needed to determine electron and hole concentrations and mobility above 50 K. The absence of SdH oscillations of hole-like charge carriers is likely due to its lower mobility, a shift of the Fermi level (unintended doping), and inaccurate band structure calculations. In addition, SdH oscillation will be zero when $g\mu^* = 1$ because of the spin reduction factor $R_{\mathrm{s}} = \cos(\pi g\mu^*/2)$. The curvature factor around the extremal cross-sectional area of the Fermi surface also affects the oscillation amplitude (see Appendix in [62]).

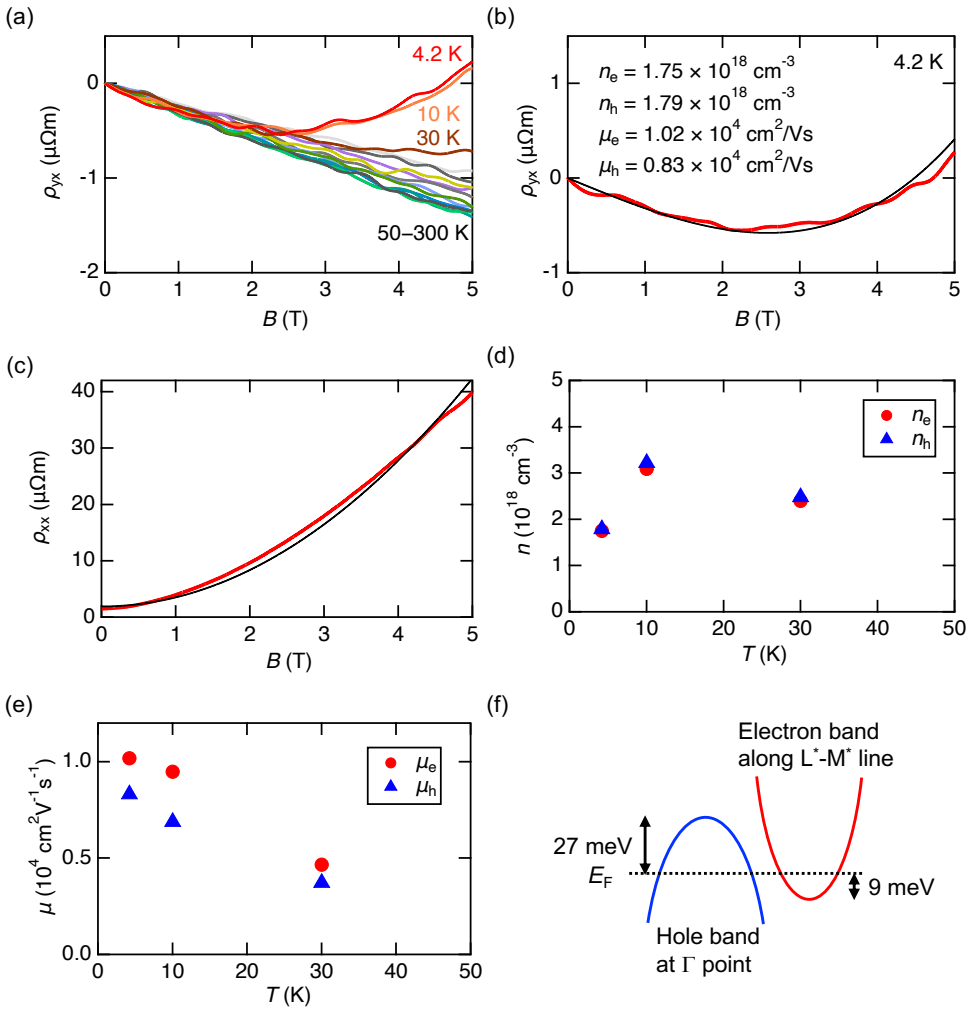

FIG. 5. (a) ρ_{yx} vs. B for Mg_3Bi_2 at various Ts. (b and c) ρ_{yx} and ρ_{xx} vs. B at 4.2 K. The black solid line represents the fitting results based on the two-band model. The parameter for fitting is denoted in the inset of (b). (d and e) n and μ vs. T obtained from the two-band model below 30 K. (f) Schematic representation of electron and hole bands with respect to Fermi level (E_F) at 30 K.

Nernst coefficient

Figure 6(a) shows the Nernst thermopower versus B. The Nernst thermopower displayed an unsaturated linear trend up to 5 T. Figure 6(b) shows the T dependence of the Nernst thermopower at 3 T (it increased with the decreasing temperature, except for 4.2 K), and the maximum value reached 40 μV/K at 10 K. Moreover, the isotropic nature of the Nernst coefficient was observed.

The Nernst thermopower was calculated for a detailed discussion. First, we evaluated the reduced potential depth (ξ) from the electron and hole band edge to the Fermi level using the measured n_e and n_h using the following relationship [19]:

$$n = 2\left(\frac{2\pi m_d{}^* k_B T}{h^2}\right)^{3/2} F_{1/2}(\xi), \qquad (6)$$

where n, $m_d{}^*$, k_B, h, and $F_{1/2}$ are the charge carrier concentration (n_e or n_h), density-of-states effective mass, Boltzmann constant, Planck constant, and Fermi–Dirac integral of the order 1/2, respectively. The n_e and n_h were obtained by two-band analysis of ρ_{xx} and ρ_{yx} under a magnetic field, as described above. The band effective mass was obtained using first-principles calculations: (m_X, m_Y, m_z) = (0.148, 0.425, 0.191) for the electron bands and (m_x, m_y, m_z) = (0.985, 1.191, 0.017) for the hole band. Here, X and Y correspond to the minor and major axes of the Fermi surface of the elliptical electron, respectively. Then, $m_d{}^* = N_d{}^{\frac{2}{3}}(m_x m_y m_z)^{\frac{1}{3}}$, where N_d is the band degeneracy, was calculated at 0.756 and 0.271 for electron and hole, respectively. At 30 K, the potential depth from the electron and hole band edge to the Fermi level were calculated at 9 and 27 meV with a band overlapping of 36 meV, as schematically shown in Fig 5(f). Notably, the effective mass of the hole band along the k_x and k_y directions was not small because it was calculated within the range of 0.1 eV from the Fermi energy. As shown in Fig. 4, the hole band below the Fermi energy has a heavy effective mass.

The partial Seebeck and Nernst coefficients of electron and hole were calculated as follows [59,63]:

$$S = \pm\frac{k_B}{e}\left\{\frac{I_{K0}I_{K1} + I_{H0}I_{H1}}{I_{K0}^2 + I_{H0}^2} - \xi\right\} \qquad (7)$$

$$NB = \frac{k_B}{e}\left\{\frac{I_{K0}I_{H1} - I_{H0}I_{K1}}{I_{K0}^2 + I_{H0}^2}\right\} \qquad (8)$$

$$I_{Ks} = \int_0^\infty \frac{x^{s+r+\frac{3}{2}}}{1 + (\omega_c\tau_0 x^r)^2}\frac{\exp(x-\xi)}{\{\exp(x-\xi)+1\}^2}\,dx \qquad (9)$$

$$I_{Hs} = \int_0^\infty \frac{\omega_c\tau_0 x^{s+2r+\frac{3}{2}}}{1 + (\omega_c\tau_0 x^r)^2}\frac{\exp(x-\xi)}{\{\exp(x-\xi)+1\}^2}\,dx \qquad (10)$$

$$x = \frac{\varepsilon}{k_B T} \qquad (11)$$

$$\omega_c = \frac{eB}{m^*} \qquad (12)$$

where ω_c and x are the cyclotron frequency and reduced charge carrier energy, respectively. The relaxation time τ_ε takes the following form:

$$\tau_\varepsilon = \tau_0\left(\frac{\varepsilon}{k_B T}\right)^r \qquad (13)$$

where the exponent $r = -1/2$ for acoustic phonon scattering and τ_0 is a factor of proportionality. The magnitude of the magnetic field was expressed using the following relationship:

$$B = \frac{\omega_c\tau_0}{\mu} \qquad (14)$$

where μ is the charge carrier mobility, which is obtained from the two-band analysis.

The total Nernst coefficient at low magnetic fields was calculated using partial Seebeck and Nernst coefficients formulas follows [59]:

$$N = \frac{N_e\{\sigma_e(\sigma_e+\sigma_h)\} + N_h\{\sigma_h(\sigma_e+\sigma_h)\} + \sigma_e\sigma_h(S_e - S_h)(R_e\sigma_e - R_h\sigma_h)}{(\sigma_e + \sigma_h)^2} \quad (15)$$

where N_e and N_h are the electron and hole Nernst coefficients, σ_e and σ_h are the electron and hole conductivities, S_e and S_h are the electron and hole Seebeck coefficients, and R_e and R_h are the electron and hole Hall coefficients, respectively. The calculated Nernst thermopower is shown in Fig. 6(a). There was a reasonable agreement between the calculations and the experiment at low magnetic fields. The ratio of the three numerators in the formula of the Nernst coefficient was 0.07:0.02:0.91, indicating that the Nernst thermopower of Mg_3Bi_2 was primarily governed by the anisotropy of the electron and hole Seebeck coefficients rather than by the partial Nernst coefficients. Note that the calculated Seebeck coefficient, $S = (\sigma_e S_e + \sigma_h S_h)/(\sigma_e + \sigma_h)$, is −31 μV/K at 30 K, in agreement with the measured one (Fig. 1(c)), indicating the validity of the calculation parameters. Here, we calculated Nernst thermopower at 30 K because we could evaluate the partial charge carrier concentrations and mobility from the two-band analysis at low temperatures. However, below 10 K, the assumption of acoustic phonon scattering is not sufficient. Notably, the measured Nernst thermopower of our crystal was slightly lower than that of a previous report on polycrystals [25]. This was probably due to the difference in chemical potential, as the Nernst and Seebeck coefficients were sensitive to chemical potential [64]. The chemical potential dependence of the Nernst coefficient of Mg_3Bi_2 will be investigated subsequently.

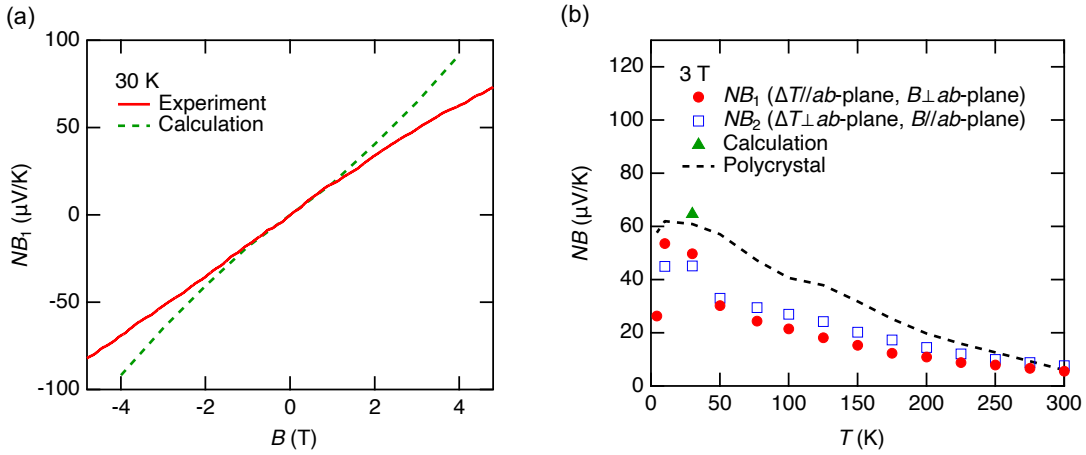

FIG. 6. (a) Measured and calculated Nernst thermopower (*NB*) vs. *B* of Mg_3Bi_2 at 30 K. (b) Nernst thermopower at 3 T measured along the in-plane and cross-plane directions. Nernst thermopower of a polycrystal is also plotted for comparison [25].

Conclusion

We demonstrated the magnetotransport properties of melt-grown n-type Mg_3Bi_2 single crystals. The MR reached 5000% at an 8 T field. Based on the SdH oscillations, we have resolved the bulk Fermi surface of Mg_3Bi_2 exhibiting large and linear MR and low effective mass. Isotropic

SdH frequency and Hall resistivity measurements suggest that SdH oscillations originate from trivial electron bands. We believe that it is possible to exploit a nontrivial band in transport properties by shifting the Fermi level upward. The two-band analysis of ρ_{xx} and ρ_{yx} confirmed the high charge carrier mobility of Mg_3Bi_2 crystals. The obtained parameters were used to reproduce other transport coefficients, such as the Nernst coefficient. These results are critical for elucidating the electronic structure and transport properties of Mg_3Bi_2.

Acknowledgment

This study was partly supported by the New Energy and Industrial Technology Development Organization (NEDO) project (Project No. JPNP14004), JSPS KAKENHI (No. 23K17342 and 20KK0124), the Murata Science Foundation, and the JST Mirai Program (No. JPMJMI19A1). JPH acknowledges support from the U.S. Department of Energy Grant #DE-SC0020923 "Discovery of goniopolar materials with zero-field Hall and Nernst effect." MANA is supported by World Premier International Research Center Initiative (WPI), MEXT, Japan

Reference

[1] A. A. Burkov, Topological Semimetals, Nature Mater. 15, 1145 (2016).
[2] B. Yan and C. Felser, Topological Materials: Weyl Semimetals, Annu. Rev. Condens. Matter Phys. 8, 337 (2017).
[3] A. A. Burkov, M. D. Hook, and L. Balents, Topological Nodal Semimetals, Phys. Rev. B 84, 235126 (2011).
[4] C. Fang, Y. Chen, H.-Y. Kee, and L. Fu, Topological Nodal Line Semimetals with and without Spin-Orbital Coupling, Phys. Rev. B 92, 081201(R) (2015).
[5] C.-K. Chiu, J. C. Y. Teo, A. P. Schnyder, and S. Ryu, Classification of Topological Quantum Matter with Symmetries, Rev. Mod. Phys. 88, 035005 (2016).
[6] C.-K. Chiu and A. P. Schnyder, Classification of Reflection-Symmetry-Protected Topological Semimetals and Nodal Superconductors, Phys. Rev. B 90, 205136 (2014).
[7] C. Fang, H. Weng, X. Dai, and Z. Fang, Topological Nodal Line Semimetals, Chinese Phys. B 25, 117106 (2016).
[8] S. Li, Z.-M. Yu, Y. Liu, S. Guan, S.-S. Wang, X. Zhang, Y. Yao, and S. A. Yang, Type-II Nodal Loops: Theory and Material Realization, Phys. Rev. B 96, 081106(R) (2017).
[9] X. Zhang, L. Jin, X. Dai, and G. Liu, Topological Type-II Nodal Line Semimetal and Dirac Semimetal State in Stable Kagome Compound Mg3Bi2, J. Phys. Chem. Lett. 8, 4814 (2017).
[10] G. Bian, T.-R. Chang, R. Sankar, S.-Y. Xu, H. Zheng, T. Neupert, C.-K. Chiu, S.-M. Huang, G. Chang, I. Belopolski *et al.*, Topological nodal-line fermions in spin-orbit metal PbTaSe2, Nat. Commun. **7**, 10556 (2016).
[11] Y. Wu, L.-L. Wang, E. Mun, D. D. Johnson, D. Mou, L. Huang, Y. Lee, S. L. Bud'ko, P. C. Canfield, and A. Kaminski, Dirac node arcs in PtSn4, Nat. Phys. **12**, 667 (2016).

[12] S. Li, Z. Guo, D. Fu, X.-C. Pan, J. Wang, K. Ran, S. Bao, Z. Ma, Z. Cai, R. Wang et al., Evidence for a Dirac Nodal-Line Semimetal in SrAs3, Science Bulletin 63, 535 (2018).

[13] M. M. Hosen, G. Dhakal, B. Wang, N. Poudel, K. Dimitri, F. Kabir, C. Sims, S. Regmi, K. Gofryk, D. Kaczorowski et al., Experimental Observation of Drumhead Surface States in SrAs3, Sci Rep 10, 2776 (2020).

[14] L. M. Schoop, M. N. Ali, C. Straßer, A. Topp, A. Varykhalov, D. Marchenko, V. Duppel, S. S. P. Parkin, B. V. Lotsch, and C. R. Ast, Dirac Cone Protected by Non-Symmorphic Symmetry and Three-Dimensional Dirac Line Node in ZrSiS, Nat. Commun. 7, 11696 (2016).

[15] J. Hu, Z. Tang, J. Liu, X. Liu, Y. Zhu, D. Graf, K. Myhro, S. Tran, C. N. Lau et al., Evidence of Topological Nodal-Line Fermions in ZrSiSe and ZrSiTe, Phys. Rev. Lett. 117, 016602 (2016).

[16] M. Neupane, I. Belopolski, M. M. Hosen, D. S. Sanchez, R. Sankar, M. Szlawska, S.-Y. Xu, K. Dimitri, N. Dhakal, P. Maldonado et al., Observation of Topological Nodal Fermion Semimetal Phase in ZrSiS, Phys. Rev. B 93, 201104(R) (2016).

[17] M. Zhao, Z.-Y. Zhuang, F. Wu, P. Leng, N. B. Joseph, X. Xie, M. Ozerov, S. He, Y. Chen, A. Narayan et al., Observation of Type-II Topological Nodal-Line Fermions in ZrSiSe, ACS Nano 18, 16684 (2024).

[18] T.-R. Chang, I. Pletikosic, T. Kong, G. Bian, A. Huang, J. Denlinger, S. K. Kushwaha, B. Sinkovic, H.-T. Jeng, T. Valla et al., Realization of a Type-II Nodal-Line Semimetal in Mg3Bi2, Advanced Science 6, 1800897 (2019).

[19] J. Mao, H. Zhu, Z. Ding, Z. Liu, G. A. Gamage, G. Chen, and Z. Ren, High Thermoelectric Cooling Performance of N-Type Mg3Bi2-Based Materials, Science 365, 495 (2019).

[20] Y. Pan, M. Yao, X. Hong, Y. Zhu, F. Fan, K. Imasato, Y. He, C. Hess, J. Fink, J. Yang et al., Mg3(Bi,Sb)2 Single Crystals towards High Thermoelectric Performance, Energy Environ. Sci. 13, 1717 (2020).

[21] Z. Liu, W. Gao, H. Oshima, K. Nagase, C.-H. Lee, and T. Mori, Maximizing the Performance of N-Type Mg3Bi2 Based Materials for Room-Temperature Power Generation and Thermoelectric Cooling, Nat. Commun. 13, 1120 (2022).

[22] N. Chen, H. Zhu, G. Li, Z. Fan, X. Zhang, J. Yang, T. Lu, Q. Liu, X. Wu, Y. Yao et al., Improved Figure of Merit (z) at Low Temperatures for Superior Thermoelectric Cooling in Mg3(Bi,Sb)2, Nat. Commun. 14, 4932 (2023).

[23] A. Li, Y. Wang, Y. Li, X. Yang, P. Nan, K. Liu, B. Ge, C. Fu, and T. Zhu, High Performance Magnesium-Based Plastic Semiconductors for Flexible Thermoelectrics, Nat. Commun. 15, 5108 (2024).

[24] P. Zhao, W. Xue, Y. Zhang, S. Zhi, X. Ma, J. Qiu, T. Zhang, S. Ye, H. Mu, J. Cheng et al., Plasticity in Single-Crystalline Mg3Bi2 Thermoelectric Material, Nature 631, 777 (2024).

[25] T. Feng, P. Wang, Z. Han, L. Zhou, W. Zhang, Q. Liu, and W. Liu, Large Transverse and Longitudinal Magneto-Thermoelectric Effect in Polycrystalline Nodal-Line Semimetal Mg3Bi2, Advanced Materials 34, 2200931 (2022).
[26] T. Feng, P. Wang, Z. Han, L. Zhou, Z. Wang, W. Zhang, Q. Liu, and W. Liu, Giant Transverse Thermoelectric Effect Induced by Topological Transition in Polycrystalline Dirac Semimetal Mg3Bi2, Energy Environ. Sci. 16, 1560 (2023).
[27] J. Xin, G. Li, G. Auffermann, H. Borrmann, W. Schnelle, J. Gooth, X. Zhao, T. Zhu, C. Felser, and C. Fu, Growth and Transport Properties of Mg3X2 (X = Sb, Bi) Single Crystals, Materials Today Physics 7, 61 (2018).
[28] S. H. Kim, C. M. Kim, Y.-K. Hong, K. I. Sim, J. H. Kim, T. Onimaru, T. Takabatake, and M.-H. Jung, Thermoelectric Properties of Mg3Sb2−xBix Single Crystals Grown by Bridgman Method, Mater. Res. Express 2, 055903 (2015).
[29] T. Zhou, XG Zhu, M Tong, Y Zhang, XB Luo, X Xie, W Feng, Q Chen, S Tan, ZY Wang, and T Jiang, Experimental Evidence of Topological Surface States in Mg3Bi2 Films Grown by Molecular Beam Epitaxy, Chinese Phys. Lett. 36, 117303 (2019).
[30] T. Zhou, M. Tong, Y. Zhang, X. Xie, Z.-Y. Wang, T. Jiang, X.-G. Zhu, and X.-C. Lai, Topological Phase Transition in Sb-Doped Mg3Bi2 Monocrystalline Thin Films, Phys. Rev. B 103, 125405 (2021).
[31] Q. Wang, F. Li, S. Xia, J. Liu, X. Liu, L. Chen, and C. Zhang, In-Situ Loading Bridgman Growth of Mg3Bi1.49Sb0.5Te0.01 Bulk Crystals for Thermoelectric Applications, Adv. Elect. Materials 8, 2101125 (2022).
[32] Q.-Q. Wang, K.-F. Liu, Y.-Y. Su, X.-C. Liu, Q. Liu, S. Zhou, J. Liu, and S.-Q. Xia, High Thermoelectric Performance and Anisotropy Studies of N-Type Mg3Bi2-Based Single Crystal, Acta Materialia 255, 119028 (2023).
[33] Y. Goto, H. Usui, M. Murata, J. E. Goldberger, J. P. Heremans, and C.-H. Lee, Band Anisotropy Generates Axis-Dependent Conduction Polarity of Mg3Sb2 and Mg3Bi2, Chem. Mater. 36, 2018 (2024).
[34] S. Kawaguchi, M. Takemoto, K. Osaka, E. Nishibori, C. Moriyoshi, Y. Kubota, Y. Kuroiwa, K. Sugimoto, High-throughput powder diffraction measurement system consisting of multiple MYTHEN detectors at beamline BL02B2 of SPring-8. Rev. Sci. Instrum. 88, 085111 (2017).
[35] F. Izumi, K. Momma, Three-dimensional Visualization in Powder Diffraction. Solid State Phenom. Solid State Phenom. 130, 15 (2007).
[36] P. Blaha, K. Schwarz, F. Tran, R. Laskowski, G.K.H. Madsen and L.D. Marks, WIEN2k: An APW+lo program for calculating the properties of solids, J. Chem. Phys. **152**, 074101 (2020).
[37] A. D. Becke, E. R. Johnson, A simple effective potential for exchange, J. Chem. Phys. **124**, 221101 (2006).
[38] F. Tran and P. Blaha, Accurate Band Gaps of Semiconductors and Insulators with a Semilocal Exchange-Correlation Potential, Phys. Rev. Lett. **102**, 226401 (2009).

[39] E. Zintl and E. Husemann, Bindungsart Und Gitterbau Binärer Magnesiumverbindungen, Zeitschrift Für Physikalische Chemie 21B, 138 (1933).

[40] See Supplemental Material at [URL will be inserted by publisher] for the optical microscopy image; EDX-based elemental mapping; SXRD pattern; laboratory XRD pattern; thermal conductivity and thermoelectric figure of merit; MR measured along different directions; oscillatory component of MR and FFT spectrum measured along different directions; oscillatory component of σ_{xx} with the Landau level indices; the frequency shifts of the SdH oscillation; cross-sectional areas of the Fermi surface obtained by first-principles calculations.

[41] V. Chopra, R. K. Ray, S. M. Bhagat. Low-temperature resistivity of Bi and its alloys. Phys. Stat. Sol. (a) **4**, 205 (1971).

[42] T. Terashima, C. Terakura, S. Uji, H. Aoki, Y. Echizen, and T. Takabatake, Resistivity, Hall effect, and Shubnikov–de Haas oscillations in CeNiSn, Phys. Rev. B **66**, 075127 (2002).

[43] R. D. Brown, Shubnikov-de Haas Measurements in Bismuth, Phys. Rev. B 2, 928 (1970).

[44] D. Shoenberg, Magnetic Oscillations in Metals (Cambridge University Press, Cambridge, 1984).

[45] F. E. Richards, Investigation of the Magnetoresistance Quantum Oscillations in Magnesium, Phys. Rev. B **8**, 2552 (1973).

[46] T. Terashima, H. T. Hirose, D. Graf, Y. Ma, G. Mu, T. Hu, K. Suzuki, S. Uji, and H. Ikeda, Fermi Surface with Dirac Fermions in CaFeAsF Determined via Quantum Oscillation Measurements, Phys. Rev. X **8**, 011014 (2018).

[47] G. P. Mikitik and Y. V. Sharlai, Manifestation of Berry's Phase in Metal Physics, Phys. Rev. Lett. **82**, 2147 (1999).

[48] G. P. Mikitik and Y. V. Sharlai, Semiclassical Energy Levels of Electrons in Metals with Band Degeneracy Lines, Sov. Phys. JETP **87**, 747 (1998).

[49] T. Liang, Q. Gibson, M. N. Ali, M. Liu, R. J. Cava, and N. P. Ong, Ultrahigh Mobility and Giant Magnetoresistance in the Dirac Semimetal Cd3As2, Nature Mater 14, 280 (2015)

[50] K. S. Novoselov, A. K. Geim, S. V. Morozov, D. Jiang, M. I. Katsnelson, I. V. Grigorieva, S. V. Dubonos, and A. A. Firsov, Two-dimensional gas of massless Dirac fermions in graphene, Nature 438, 197 (2005).

[51] D.-X. Qu, Y. S. Hor, J. Xiong, R. J. Cava, and N. P. Ong, Quantum oscillations and hall anomaly of surface states in the topological insulator Bi2Te3, Science 329, 821 (2010).

[52] Z. Wang, Y. Zheng, Z. Shen, Y. Lu, H. Fang, F. Sheng, Y. Zhou, X. Yang, Y. Li, C. Feng, and Z.-A. Xu, Helicity-protected ultrahigh mobility Weyl fermions in NbP, Phys. Rev. B 93, 121112 (2016).

[53] Y. Ando, Topological Insulator Materials, J. Phys. Soc. Jpn. 82, 102001 (2013).

[54] A. Alexandradinata, C. Wang, W. Duan, and L. Glazman, Revealing the Topology of Fermi-Surface Wave Functions from Magnetic Quantum Oscillations, Phys. Rev. X **8**, 011027 (2018).

[55] C. Schindler, D. Gorbunov, S. Zherlitsyn, S. Galeski, M. Schmidt, J. Wosnitza, and J. Gooth, Strong anisotropy of the electron-phonon interaction in NbP probed by magnetoacoustic quantum oscillations, Phys. Rev. B **102**, 165156 (2020).

[56] C. Guo et al., Temperature Dependence of Quantum Oscillations from Non-Parabolic Dispersions, Nat Commun 12, 6213 (2021).

[57] J. S. Kang, D. Vu, and J. P. Heremans, Identifying the Dirac Point Composition in Bi1−xSbx Alloys Using the Temperature Dependence of Quantum Oscillations, J. Appl. Phys. 130, 225106 (2021).

[58] T. Terashima, S. Uji, T. Wang, and G. Mu, Topological frequency shift of quantum oscillation in CaFeAsF, npj Quantum Mater. **7**, 25 (2022).

[59] E. H. Putley, The Hall Effect and Related Phenomena (Butterworth & Co., London 1960).

[60] P. M. C. Rourke, A. F. Bangura, C. Proust, J. Levallois, N. Doiron-Leyraud, D. LeBoeuf, L. Taillefer, S. Adachi, M. L. Sutherland, and N. E. Hussey, Fermi-Surface Reconstruction and Two-Carrier Model for the Hall Effect in $YBa_2Cu_4O_8$. Phys. Rev. B: 82, 020514 (2010).

[61] C.-Z. Li, J.-G. Li, L.-X. Wang, L. Zhang, J.-M. Zhang, D. Yu, and Z.-M. Liao, Two-Carrier Transport Induced Hall Anomaly and Large Tunable Magnetoresistance in Dirac Semimetal Cd_3As_2 Nanoplates, ACS Nano 10, 6020 (2016).

[62] H. Aoki, N. Kimura, T. Terashima, Fermi Surface Properties, Metamagnetic Transition and Quantum Phase Transition of $CeRu_2Si_2$ and Its Alloys Probed by the dHvA Effect, J. Phys. Soc. Jpn. 83, 072001 (2014).).

[63] Y. Hasegawa, T. Komine, Y. Ishikawa, A. Suzuki, and H. Shirai, Numerical Calculation of Magneto-Seebeck Coefficient of Bismuth under a Magnetic Field, Jpn. J. Appl. Phys. 43, 35 (2004).

[64] M. Murata, K. Nagase, K. Aoyama, N. Abe, and A. Yamamoto, Influence of Carrier Doping on Thermo- and Galvano-Magnetic Effects of Bi88Sb12 Alloys, Journal of Applied Physics 134, 215103 (2023).